OPTICA

In situ tuning of optomechanical crystals with nano-oxidation

Utku Hatipoglu,[1,2,†] Sameer Sonar,[1,2,†] David P. Lake,[1,2] Srujan Meesala,[1,2] and Oskar Painter[1,2,3,*]

[1]*Institute for Quantum Information and Matter, California Institute of Technology, Pasadena, California 91125, USA*
[2]*Kavli Nanoscience Institute and Thomas J. Watson, Sr., Laboratory of Applied Physics, California Institute of Technology, Pasadena, California 91125, USA*
[3]*AWS Center for Quantum Computing, Pasadena, California 91125, USA*
[†]*These authors contributed equally to this work.*
*opainter@caltech.edu

Optomechanical crystals are a promising device platform for quantum transduction and sensing. Precise targeting of the optical and acoustic resonance frequencies of these devices is crucial for future advances on these fronts. However, fabrication disorder in these wavelength-scale nanoscale devices typically leads to inhomogeneous resonance frequencies. Here we achieve *in situ*, selective frequency tuning of optical and acoustic resonances in silicon optomechanical crystals via electric field-induced nano-oxidation using an atomic-force microscope. Our method can achieve a tuning range >2 nm (0.13%) for the optical resonance wavelength in the telecom C-band, and >60 MHz (1.2%) for the acoustic resonance frequency at 5 GHz. The tuning resolution of 1.1 pm for the optical wavelength and 150 kHz for the acoustic frequency allows us to spectrally align multiple optomechanical crystal resonators using a pattern generation algorithm. Our results establish a method for precise post-fabrication tuning of optomechanical crystals. This technique can enable coupled optomechanical resonator arrays, scalable resonant optomechanical circuits, and frequency matching of microwave-optical quantum transducers. © 2024 Optica Publishing Group under the terms of the Optica Open Access Publishing Agreement

https://doi.org/10.1364/OPTICA.516479

1. INTRODUCTION

Optomechanical crystals (OMCs) provide a coherent interface between optical photons and acoustic phonons [1]. This capability is now being utilized in microwave-optical quantum transducers [2–6] towards connecting gigahertz frequency superconducting quantum processors [7] via low-loss optical communication channels. In parallel efforts, OMCs have enabled coherent control and routing of phonons in chip-scale optomechanical circuits [8–10] with demonstrations of nonreciprocal optical transmission [11] and topologically protected phonon transport [12]. However, scaling to multi-node quantum networks and more complex optomechanical circuits is challenging due to variations in optical and acoustic resonance frequencies across devices caused by fabrication imperfections. In particular, since critical feature sizes in OMCs are affected by the precision limits of electron beam lithography and reactive ion etching, the spread in resonance frequencies across devices can be more than a hundred times the resonance linewidths, thereby hindering frequency alignment.

Post-fabrication tuning of optical resonance frequencies in chip-scale microcavities has been achieved using a variety of techniques including laser-assisted thermal oxidation [13], strain tuning [14,15], thermo-optic tuning [16,17], and gas condensation [18,19]. The atomic force microscope (AFM) nano-oxidation

technique has been used to realize polarization degenerate microcavities [20] and to create low-loss microcavities from line defects in a photonic crystal [21]. However, since OMCs co-localize optical and acoustic resonances in a wavelength-scale volume, selective tuning of both optical and acoustic resonances without adding significant scattering losses is a complex endeavor and an outstanding technical challenge. Here we use AFM nano-oxidation tuning to demonstrate such control over the resonance frequencies of OMCs. In our approach, field-induced oxidation of the silicon device surface with high spatial resolution allows us to tune the acoustic resonance by modifying the local mass distribution and elasticity, and the optical resonance by modifying the local refractive index. By using a pattern generation algorithm to guide the nano-oxidation sequence in real-time, we achieve simultaneous alignment of the optical and acoustic resonance frequencies of multiple OMC cavities.

2. AFM NANO-OXIDATION SETUP

A simplified schematic of the experimental setup is shown in Fig. 1(a). We perform nano-oxidation using a conductive chromium/platinum coated silicon AFM tip with a radius <25 nm [22] and track the optical and acoustic resonances in real-time by
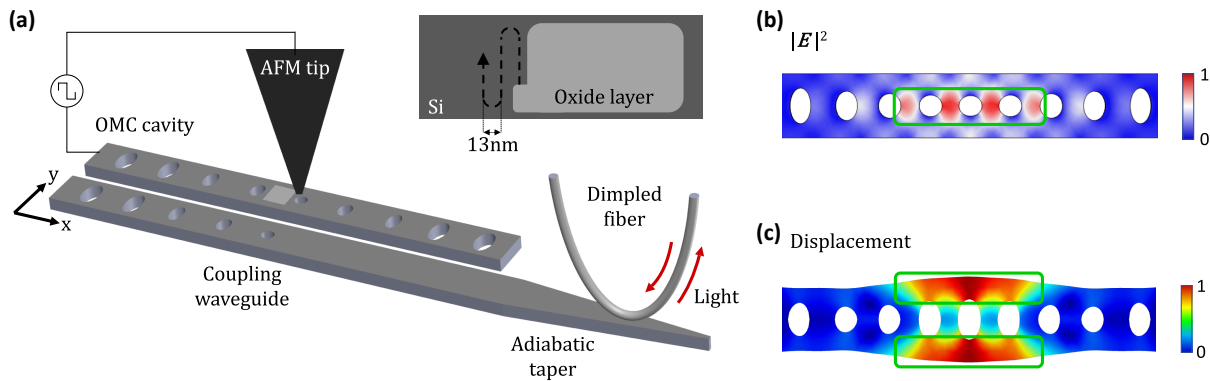
Fig. 1. Nano-oxidation setup schematic and OMC cavity mode profiles. (a) Simplified schematic of the AFM nano-oxidation setup. The AFM tip is used to perform nano-oxidation while measuring the optical and acoustic resonances of the device in real-time with a dimpled optical fiber. The AFM tip is operated in tapping mode over a grounded silicon sample and biased with a square wave voltage, allowing for electrochemical formation of an oxide layer on the silicon surface. The inset illustrates the raster scan used to generate the oxide layer. (b) Electric field intensity profile of the optical mode. The optics-focused oxidation region is outlined in green. (c) Displacement magnitude profile of the acoustic breathing mode. The acoustics-focused oxidation regions are outlined in green.

performing optomechanical spectroscopy via a dimpled optical fiber coupled to the device [23]. The AFM is operated in tapping mode while a voltage bias is applied to the conductive tip, and the silicon-on-insulator (SOI) chip with a silicon device layer resistivity of 5 kΩ-cm is grounded. When the voltage-biased AFM tip is brought close to the silicon surface, a strong electric field triggers an electrochemical reaction between ions in the native water meniscus and the silicon surface, resulting in local oxidation of silicon. Importantly, this reaction can proceed even when the silicon surface is covered with native oxide, because the strong local electric field allows oxyanions (OH^-, O^-) to diffuse through the native oxide [24]. In our experiments, we maintain the AFM setup enclosure at ambient conditions with a relative humidity of $40 \pm 5\%$ and temperature of $23 \pm 1°C$, and apply a square wave voltage oscillating between ±10 V at a frequency of 20 Hz to the AFM tip.

The OMC cavities in this work were fabricated on an SOI chip with a 220 nm thick silicon device layer. The cavities were patterned via electron beam lithography followed by reactive ion etching, and finally suspended by removing the buried oxide layer with an anhydrous vapor hydrofluoric acid etch. The devices were designed to support a fundamental TE-like optical resonance at a wavelength of ∼1550 nm and a breathing acoustic resonance at a frequency of ∼ 5.1 GHz [Figs. 1(b) and 1(c)] [25]. An on-chip adiabatic waveguide coupler [26] allows for optical coupling to the OMC cavity using a dimpled optical fiber. The optical spectrum of the OMC cavity was probed in reflection mode, and the resonance frequencies were recorded before and after each step of the nano-oxidation sequence. To measure the acoustic spectrum of the device, we routed the optical signal reflected from the device to a high-speed photodetector and measured the power spectral density (PSD) of the photodetector electrical output on a spectrum analyzer. The result is proportional to the PSD of thermal displacement fluctuations of the acoustic mode, which are transduced onto the optical signal via the optomechanical interaction in the device. In these measurements, the laser was blue-detuned with respect to the optical resonance frequency by a detuning close to the acoustic resonance frequency and operated at low power to minimize optomechanical back-action on the acoustic mode [27].

3. NANO-OXIDATION CHARACTERIZATION

From the simulated mode profiles shown in Figs. 1(b) and 1(c), we identified two strategic oxidation regions for selective tuning of the optical and acoustic modes. Nano-oxidation in the region shown with the green rectangle in Fig. 1(b) is expected to induce a relatively large change in the optical resonance due to a high concentration of electric field energy. Here the impact on the acoustic resonance is expected to be minimal due to two reasons. First, the displacement amplitude is small in this region. Second, even though the stress amplitude is large in this region, the Young's modulus of the oxide layer when weighted by its thickness is similar to that of the original silicon. In contrast, nano-oxidation on the regions shown with the green rectangles in Fig. 1(c) leads to a large acoustic resonance shift and a small optical wavelength shift due to the high concentration of motional mass and low concentration of electric field energy. In Section D of Supplement 1, we show the results of finite element method (FEM) simulations where we investigated the optical and acoustic frequency shifts due to creation of an oxide pixel at an arbitrary location on the OMC surface. This allowed us to identify candidate regions for fine tuning of optical and acoustic resonance frequencies with maximal selectivity. For coarse frequency tuning, we opted to use larger, rectangular oxide patterns instead of oxide pixels to maximize the tuning range at the expense of selectivity.

Prior to experiments on OMC devices, we characterized the effect of the AFM tapping amplitude and scanning velocity on nano-oxidation using a bare silicon chip. We observed that lower tapping amplitude and slower scanning velocities result in wider and thicker oxide lines. We measured the three-dimensional profiles of field-induced oxide lines and pixels using AFM measurements as described in Section B of Supplement 1. Based on the amount of frequency tuning required, we operated the AFM in two distinct modes, which we refer to as "mild" and "aggressive" tuning modes. In the mild tuning mode, the tapping amplitude and scan speed were set to 15 nm and 100 nm/s, respectively, resulting in oxide thickness of approximately 1.2 nm. In the aggressive tuning mode, the tapping amplitude and scan speed were set to 5 nm and 50 nm/s, respectively, leading to oxide thickness of approximately 2.5 nm. In the mild tuning mode, nano-oxidation was found to generate single pixels with a lateral size of approximately 25 nm.

In order to obtain thicker and more uniform oxide patterns with a raster scan, we used a line spacing of 13 nm with significant overlap between neighboring lines as illustrated in the inset of Fig. 1(a). This procedure allowed us to generate oxide layers with a thickness of 1.6 nm and 3.2 nm in the mild and aggressive tuning modes, respectively. We note that we can get oxide layers with a thickness greater than 10 nm by operating the AFM in the contact mode where the AFM cantilever tip is in contact with the substrate throughout the oxidation process. However, the contact mode is more challenging to implement in suspended structures where large attractive forces between the surface and the AFM tip can damage the OMC and destroy the resonances.

After establishing these nano-oxidation parameters, we performed optical and acoustic resonance frequency tuning experiments on a single OMC cavity. We specifically studied the impact of two oxidation patterns: (i) an optics-focused pattern [Fig. 2(a), left] composed of four rectangles located between the five central ellipses in the beam (here the lengths of the rectangles were kept constant at $l_0 = 170$ nm, while their width w was varied), and (ii) an acoustics-focused pattern [Fig. 2(a), right] composed of two rectangles situated at the edge of the OMC cavity (here the widths of the rectangles were kept fixed at $w_0 = 120$ nm, while their length l was varied). As shown in Fig. 2(b), the experimentally measured tuning of the resonance frequencies (solid and dashed lines) agrees with simulation results (dotted lines). For the optics-focused pattern, increasing w leads to a large reduction in the optical wavelength and a smaller reduction in acoustic frequency. For the acoustics-focused pattern, increasing l leads to a decrease in acoustic frequency due to increasing motional mass

(a)   Optics focused pattern   Acoustic focused pattern
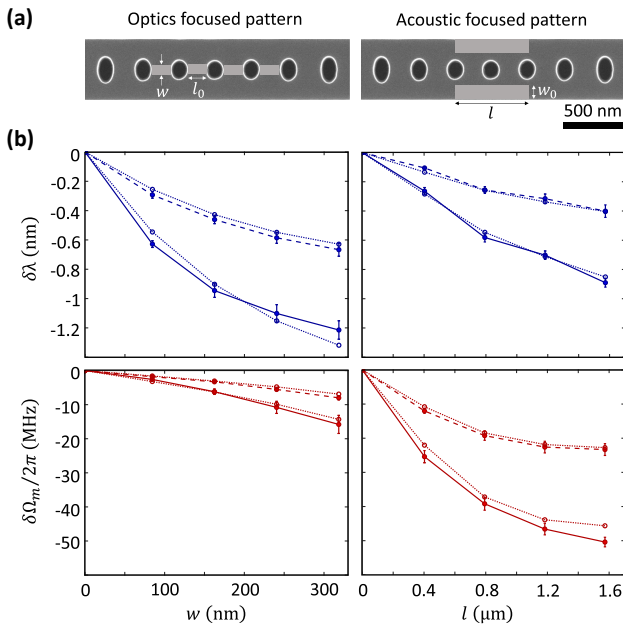
(b)

Fig. 2. Coarse frequency tuning of OMC cavity. (a) Oxidation patterns used for coarse tuning of optical (left) and acoustic (right) resonances. For the optics-focused pattern, the length is fixed at $l_0 = 170$ nm, and the width w is varied. For the acoustics-focused pattern, the width is fixed at $w_0 = 120$ nm, and the length l is varied. (b) Tuning of optical and acoustic resonances as a function of the size of the oxidation pattern. Optical wavelength shift $\delta\lambda$ with respect to w (top left) and l (top right). Acoustic frequency shift $\delta\Omega/2\pi$ with respect to w (bottom left) and l (bottom right). Solid (dashed) lines represent data taken for aggressive (mild) oxidation. Dotted lines show simulated values from finite element method simulations. Error bars represent the standard deviation across five OMC cavities measured for each dataset.

$(\Omega_m \propto \sqrt{1/m})$ and a decrease in the optical wavelength due to a decrease in the effective dielectric constant. Aggressive oxidation at $w = 320$ nm resulted in more than 1.2 nm blue shift of the optical wavelength while aggressive oxidation at $l = 1.6$ µm resulted in more than 50 MHz reduction in the acoustic frequency. In Fig. 2(b), each data point represents the average value and the standard deviation obtained from five devices. For each device, the patterns were applied cumulatively, starting from the center and adding more oxide to increase either w or l at each step.

4. SIMULTANEOUS OPTICAL AND ACOUSTIC FREQUENCY TUNING

To achieve simultaneous tuning of optical and acoustic resonances, we define a joint pattern consisting of a union of the previously introduced optics-focused and acoustics-focused patterns. This is parameterized by geometric parameters w and l, and binary variables M_O (M_A), which denote mild or aggressive oxidation in the optical (acoustic) components of the joint pattern. Using the experimental data shown in Fig. 2, we interpolate $\delta\lambda$ and $\delta\Omega_m$ as a function of the parameters $\{w, l, M_O, M_A\}$. To achieve the desired frequency shifts, we developed a pattern generation algorithm to find an optimal combination of the acoustic and optics focused patterns. The algorithm takes the desired frequency and wavelength shift as the input and generates the required joint oxidation pattern by searching for the most suitable combination of l and w. The algorithm starts the search from milder oxidation modes to minimize optical scattering losses. A maximum increase in intrinsic scattering loss of $\delta\kappa_i/2\pi = 440$ MHz has been observed for $w < 350$ nm. More details on the pattern generation algorithm and the optical scattering losses are given in Supplement 1, Sections E and C, respectively.

While the pattern generation algorithm is sufficient for coarse tuning of the OMC wavelength and frequency, fine frequency alignment to within the linewidth of the optical and acoustic resonances requires pixel-by-pixel nano-oxidation with real-time feedback. This method allows for ~1 pm precision for optical wavelength tuning and ~150 kHz precision for acoustic resonance tuning. To quantify the sensitivity of the optical resonance wavelength to single oxide pixels, we applied a pixel-by-pixel linear oxide pattern perpendicular to the OMC long axis with a pitch of 13 nm shown in the inset of Fig. 3(a). The resonance spectra recorded in Fig. 3(a) for each incremental pixel in the oxidation sequence reveal a decrease in the per-pixel wavelength shift towards the edges of the OMC, with an observed shift of -1.1 pm/px near the extreme points A and C. This spatial dependence is in agreement with predictions from FEM simulations, as discussed in Supplement 1, Section D. We perform a similar sensitivity analysis for the acoustic resonance via a pixel-by-pixel linear oxide pattern applied with a pitch of 40 nm along the edge of the OMC, shown in the inset of Fig. 3(b). The acoustic resonance spectrum is recorded after the addition of every oxide pixel, and the results are shown in Fig. 3(b). We measure a maximum frequency shift of -1 MHz/px at point A, which is in line with the center of the OMC cavity. As we move away from the center, the sensitivity eventually decreases to a value of -150 kHz/px as measured at the extreme point B.

After characterizing coarse and fine tuning of optical and acoustic resonance frequencies of a single OMC cavity, we used these techniques to perform frequency alignment of both the optical and acoustic resonances of three OMC cavities. Due to constraints
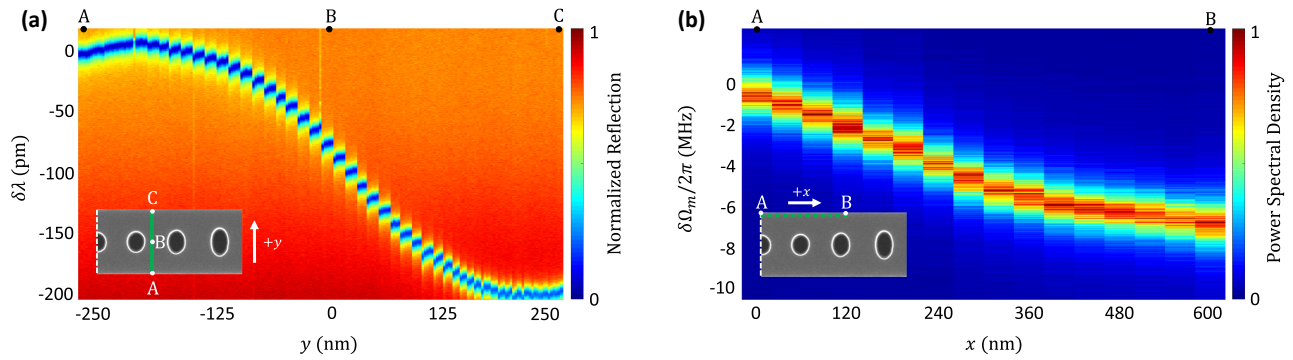
Fig. 3. Real-time, *in situ* monitoring of the oxidation process. (a) Real-time spectra showing optical resonance tuning during sequential application of the oxidation pattern. As shown in the inset, the pattern is applied starting at point A, one pixel at a time, up to point C. AFM tip locations during the experiment are shown at the top of the plot with letters A, B, and C, which correspond to the points labeled on the inset image. Discontinuities along the horizontal axis are due to proximity effects between the AFM tip and the OMC cavity during the oxidation sequence. (b) Real-time data showing acoustic frequency shift during pixel-wise oxidation. Oxide pixels are applied on the surface starting from point A up to point B as shown in the inset.
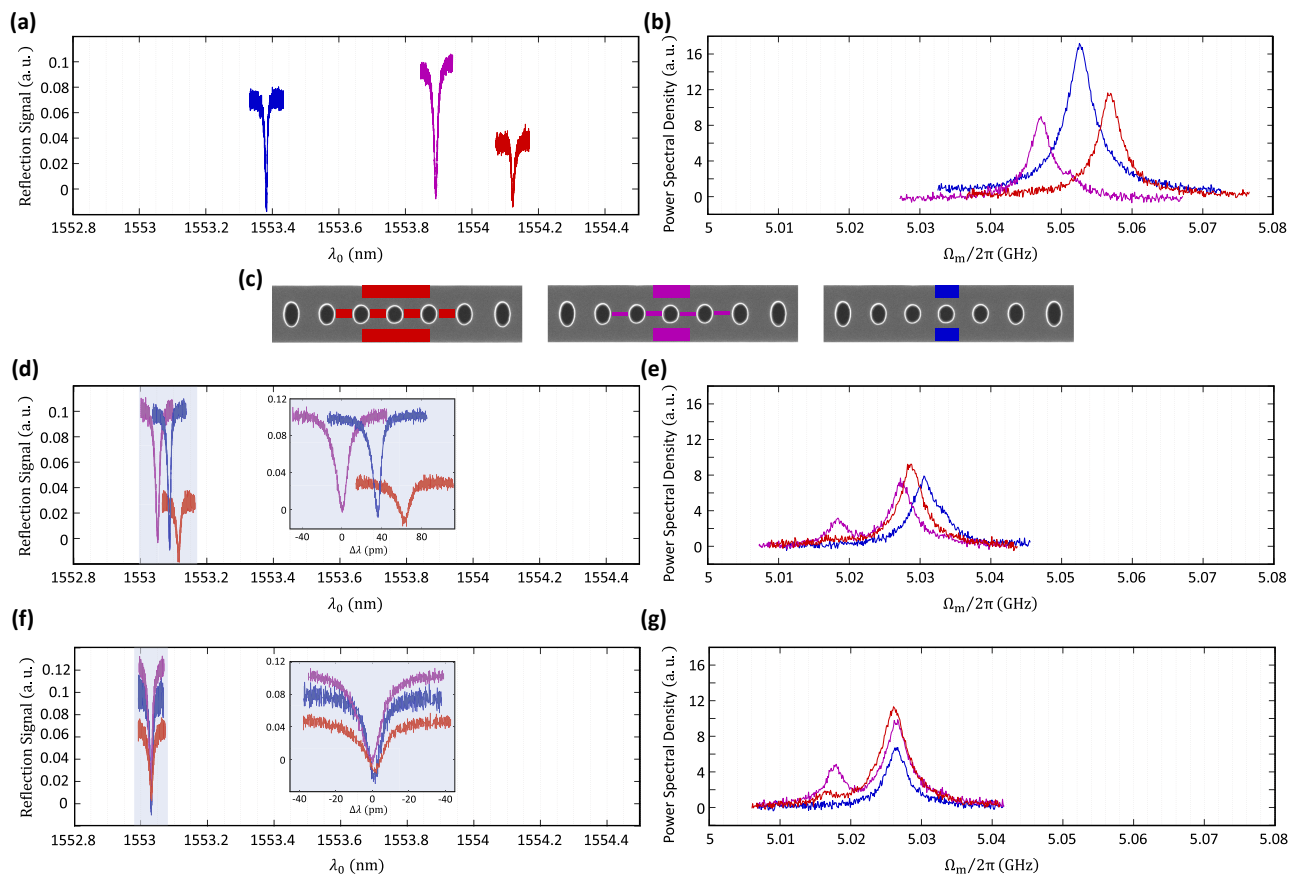

Fig. 4. Simultaneous optical and acoustic resonance frequency alignment of three OMC cavities. Initial (a) optical and (b) acoustic resonance spectra. (c) Joint patterns used for coarse alignment of the three OMC cavities. The patterns are shown with a color code matched to the OMC spectra and are applied in the order shown from left to right. Resonance frequencies were recorded after every step of the nano-oxidation protocol. (d) Optical and (e) acoustic spectra measured after completion of the coarse alignment of sequence. (f) Optical and (g) acoustic spectra after completion of the real-time fine-tuning sequence. Insets in panels (d) and (f) show a zoomed-in view of the optical resonances. The satellite acoustic resonance in magenta in panels (e) and (g) is due to a neighboring OMC cavity within the evanescent field of the optical coupling waveguide.

on the maximum achievable tuning range (see Supplement 1, Section G for details), we pre-select cavities with initial optical wavelength spread <1 nm and acoustic frequency spread <20 MHz, shown in Figs. 4(a) and 4(b). We begin with coarse tuning steps using oxidation patterns generated by the pattern generation algorithm as shown in Fig. 4(c). This aligns the optical

resonance wavelengths across all cavities to within a tolerance of <200 pm and acoustic resonance frequencies to within a tolerance of 5 MHz. The results of the coarse tuning are shown in Figs. 4(d) and 4(e). We then proceed to real-time, pixel-by-pixel oxidation with feedback to achieve fine tuning of the resonance frequencies. After four rounds of fine-tuning, the optical and acoustic resonance

frequencies were successfully tuned to within 2 pm and 500 kHz respectively [see Figs. 3(f) and 3(g)]. A step-by-step description of the frequency alignment procedure is described in detail in Supplement 1, Section F.

5. OUTLOOK

We have shown simultaneous, real-time tuning of optical and acoustic resonances in OMC cavities via AFM nano-oxidation, demonstrating optical wavelength and acoustic frequency shifts >2 nm (0.13%) and >60 MHz (1.2%), respectively. This tuning range may be improved by generating thicker oxide layers using AFM in the contact mode. Such *in situ* tuning methods could enable the realization of coupled optomechanical resonator arrays to study topological phases of photons and phonons [12,28–30]. In the context of OMC-based microwave-optical quantum transducers [2–6], the nano-oxidation tuning demonstrated here will enable post-fabrication frequency alignment of transducers in multiple nodes of a quantum network. Moreover, these techniques are applicable to other material systems such as silicon nitride [31], where tuning of optomechanical devices may be required [32]. Finally, AFM nano-oxidation could be a valuable technique for fundamental studies of two-level systems (TLS) in amorphous materials [33] by enabling spatially targeted creation of TLS in acoustic [1] and superconducting [34] devices.

Disclosures. The authors declare no conflicts of interest.

Data availability. Correspondence and requests for data should be sent to OP (opainter@caltech.edu).

Supplemental document. See Supplement 1 for supporting content.

REFERENCES

1. G. S. MacCabe, H. Ren, J. Luo, *et al.*, "Nano-acoustic resonator with ultralong phonon lifetime," Science **370**, 840–843 (2020).
2. M. Mirhosseini, A. Sipahigil, M. Kalaee, *et al.*, "Superconducting qubit to optical photon transduction," Nature **588**, 599–603 (2020).
3. S. Meesala, S. Wood, D. Lake, *et al.*, "Non-classical microwave-optical photon pair generation with a chip-scale transducer," arXiv, arXiv:2303.17684 (2023).
4. W. Jiang, F. M. Mayor, S. Malik, *et al.*, "Optically heralded microwave photon addition," Nat. Phys. **19**, 1423–1428 (2023).
5. M. J. Weaver, P. Duivestein, A. C. Bernasconi, *et al.*, "An integrated microwave-to-optics interface for scalable quantum computing," Nat. Nanotechnol. **17**, 166–172 (2024).
6. H. Zhao, A. Bozkurt, and M. Mirhosseini, "Electro-optic transduction in silicon via gigahertz-frequency nanomechanics," Optica **10**, 790–796 (2023).
7. M. Kjaergaard, M. E. Schwartz, J. Braumüller, *et al.*, "Superconducting qubits: current state of play," Annu. Rev. Condens. Matter Phys. **11**, 369–395 (2020).
8. K. Fang, M. H. Matheny, X. Luan, *et al.*, "Optical transduction and routing of microwave phonons in cavity-optomechanical circuits," Nat. Photonics **10**, 489–496 (2016).
9. R. N. Patel, Z. Wang, W. Jiang, *et al.*, "Single-mode phononic wire," Phys. Rev. Lett. **121**, 040501 (2018).
10. A. Zivari, N. Fiaschi, R. Burgwal, *et al.*, "On-chip distribution of quantum information using traveling phonons," Sci. Adv. **8**, eadd2811 (2022).
11. K. Fang, J. Luo, A. Metelmann, *et al.*, "Generalized non-reciprocity in an optomechanical circuit via synthetic magnetism and reservoir engineering," Nat. Phys. **13**, 465–471 (2017).
12. H. Ren, T. Shah, H. Pfeifer, *et al.*, "Topological phonon transport in an optomechanical system," Nat. Commun. **13**, 3476 (2022).
13. C. L. Panuski, I. Christen, M. Minkov, *et al.*, "A full degree-of-freedom spatiotemporal light modulator," Nat. Photonics **16**, 834–842 (2022).
14. C. W. Wong, P. T. Rakich, S. G. Johnson, *et al.*, "Strain-tunable silicon photonic band gap microcavities in optical waveguides," Appl. Phys. Lett. **84**, 1242–1244 (2004).
15. I. Luxmoore, E. D. Ahmadi, B. Luxmoore, *et al.*, "Restoring mode degeneracy in H1 photonic crystal cavities by uniaxial strain tuning," Appl. Phys. Lett. **100**, 121116 (2012).
16. M. S. Nawrocka, T. Liu, X. Wang, *et al.*, "Tunable silicon microring resonator with wide free spectral range," Appl. Phys. Lett. **89**, 071110 (2006).
17. A. Faraon, D. Englund, I. Fushman, *et al.*, "Local quantum dot tuning on photonic crystal chips," Appl. Phys. Lett. **90**, 213110 (2007).
18. S. Mosor, J. Hendrickson, B. Richards, *et al.*, "Scanning a photonic crystal slab nanocavity by condensation of xenon," Appl. Phys. Lett. **87**, 141105 (2005).
19. S. Strauf, M. T. Rakher, I. Carmeli, *et al.*, "Frequency control of photonic crystal membrane resonators by monolayer deposition," Appl. Phys. Lett. **88**, 043116 (2006).
20. K. Hennessy, C. Högerle, E. Hu, *et al.*, "Tuning photonic nanocavities by atomic force microscope nano-oxidation," Appl. Phys. Lett. **89**, 041118 (2006).
21. A. Yokoo, T. Tanabe, E. Kuramochi, *et al.*, "Ultrahigh-Q nanocavities written with a nanoprobe," Nano Lett. **11**, 3634–3642 (2011).
22. "AFM probe selection guide: how to choose an AFM probe," Park Systems, https://www.parksystems.com/images/media/brochures/probe/Park_AFM_ProbeGuide_190620E32AB.pdf.
23. P. E. Barclay, K. Srinivasan, M. Borselli, *et al.*, "Efficient input and output fiber coupling to a photonic crystal waveguide," Opt. Lett. **29**, 697–699 (2004).
24. R. Garcia, R. V. Martinez, and J. Martinez, "Nano-chemistry and scanning probe nanolithographies," Chem. Soc. Rev. **35**, 29–38 (2006).
25. J. Chan, A. H. Safavi-Naeini, J. T. Hill, *et al.*, "Optimized optomechanical crystal cavity with acoustic radiation shield," Appl. Phys. Lett. **101**, 081115 (2012).
26. S. Gröblacher, J. T. Hill, A. H. Safavi-Naeini, *et al.*, "Highly efficient coupling from an optical fiber to a nanoscale silicon optomechanical cavity," Appl. Phys. Lett. **103**, 181104 (2013).
27. M. Aspelmeyer, T. J. Kippenberg, and F. Marquardt, "Cavity optomechanics," Rev. Mod. Phys. **86**, 1391–1452 (2014).
28. V. Peano, C. Brendel, M. Schmidt, *et al.*, "Topological phases of sound and light," Phys. Rev. X **5**, 031011 (2015).
29. V. Peano, M. Houde, C. Brendel, *et al.*, "Topological phase transitions and chiral inelastic transport induced by the squeezing of light," Nat. Commun. **7**, 10779 (2016).
30. C. Brendel, V. Peano, O. J. Painter, *et al.*, "Pseudomagnetic fields for sound at the nanoscale," Proc. Natl. Acad. Sci. USA **114**, E3390–E3395 (2017).
31. F.-S. Chien, Y. Chou, T. Chen, *et al.*, "Nano-oxidation of silicon nitride films with an atomic force microscope: chemical mapping, kinetics, and applications," J. Appl. Phys. **89**, 2465–2472 (2001).
32. R. D. Delaney, M. D. Urmey, S. Mittal, *et al.*, "Superconducting-qubit readout via low-backaction electro-optic transduction," Nature **606**, 489–493 (2022).
33. J. Lisenfeld, A. Bilmes, S. Matityahu, *et al.*, "Decoherence spectroscopy with individual two-level tunneling defects," Sci. Rep. **6**, 23786 (2016).
34. M. Chen, J. C. Owens, H. Putterman, *et al.*, "Phonon engineering of atomic-scale defects in superconducting quantum circuits," arXiv, arXiv:2310.03929 (2023).